1-13-1989

Theoretical model for the images formed by a spherical particle in a coherent imaging system: comparison

Scott Alan Schaub
University of Nebraska - Lincoln

D. R. Alexander
University of Nebraska- Lincoln

J. P. Barton
University of Nebraska - Lincoln

Theoretical model for the image formed by a spherical particle in a coherent imaging system: comparison to experiment

S. A. Schaub
D. R. Alexander, MEMBER SPIE
J. P. Barton
University of Nebraska-Lincoln
Center for Electro-Optics
Lincoln, Nebraska 68588-0525

Abstract. A simple theoretical model is presented that allows calculation of the image produced by a spherical absorbing particle illuminated by monochromatic, coherent laser light. Results presented in this paper are restricted to a single-lens imaging system, although generalization to more complex imaging system configurations would be straightforward. The method uses classic Lorenz-Mie scattering theory to obtain the electromagnetic field external to an absorbing spherical particle and a Fourier optics approach to calculate the intensities in the image plane. Experimental results evaluating focus characteristics are examined for 50 μm diameter water droplets using an N_2 laser imaging system in conjunction with a digital image processor, and the experimental images are compared to the results of the theoretical model. Comparative focus criteria results are particularly useful in aerosol science research involving dynamic particle size measurements in which criteria for focus and depth of field must be established.

Subject terms: spray analysis; image formation; focus effects.

Optical Engineering 28(5), 565-571 (May 1989).

CONTENTS

1. INTRODUCTION

During recent years there has been a growing interest in the field of dynamic particle size measurements. Applications such as combustion optimization, industrial and agricultural spray application, and cloud simulation for aircraft icing studies all require detailed knowledge of both particle size and particle size distribution. One method commonly used to measure particle and spray characteristics utilizes laser interferometry and light scattering.[1,2] Although restricted to spherical droplets,[3] this method provides valuable size and velocity information for a variety of applications. Another method of obtaining data on particle characteristics, which is addressed in this paper, uses a laser-based imaging system coupled to a digital image processor.[4,5]

Paper 2603 received July 15, 1988; revised manuscript received Jan. 13, 1989; accepted for publication Jan. 13, 1989.

The specific imaging system under consideration has been described in detail in previous work[5,6] and can be summarized as shown in Fig. 1. In this system, an object located at plane z_0 is illuminated by an N_2 laser (Molectron model UV-12, λ = 337 nm, 2.5 mJ/pulse, 10 ns FWHM). The image is formed by passing the scattered light through a plano-convex lens (f = 50 mm, D = 25 mm) onto a vidicon tube (plane z_3). The video signal is then sent to a Recognition Concepts, Inc., Trapix 5532 digital image processor for analysis. To obtain accurate particle size data, the imaging system must be calibrated using particles of known sizes, and the calibration data must be incorporated into an automated algorithm, allowing for rapid processing of video frames containing particle images. For particles in focus, the calibration and algorithm implementation is straightforward. However, for sizing dynamic sprays, special algorithms are required since most particles in a spray are slightly defocused due to the spatial distribution of particles throughout the spray. The computer-based sizing algorithms must have the capability of determining when a particle is in focus and its correct size. Such a computer algorithm has been developed,[6,7] to count and size particles in dynamic sprays based on criteria derived from experimental calibrations using a monodisperse droplet generator and a chrome-on-glass static calibration reticle.[8] The technique makes use of the intensity gradient at the particle edge and the measured average intensity (gray level) of the particle, both of which change as the particle is moved in and out of focus. By carefully positioning particles of known size at various locations with respect to the object plane (plane z_0), we obtained an empirical criteria to determine particle size as a function of the

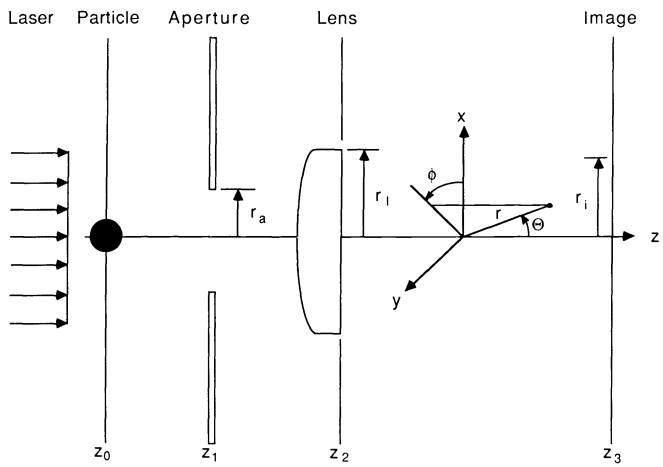

Fig. 1. Imaging system geometry.

measured average gray level of the particle. The particle edge gradient and average gray level have been shown[6,7] to provide excellent criteria on which to base in-focus and out-of-focus determination. Although empirical results can provide accurate algorithms for particle sizing for a particular optical system, a theoretical model would be useful in examining such things as the effect of changing aperture size on the observed particle images, the variation in average gray level with the degree of particle defocus, and the relationship between the actual particle edge and the observed edge intensity gradient of a defocused particle.

In a recent paper by Thompson and Malyak,[9] an approach using the Huygens-Fresnel principle was used to calculate the intensity distribution for opaque disks illuminated by a coherent laser source. Results showed that the depth of field for a coherent imaging system is much larger than for a similar incoherent system. In this paper, we consider the more general case of a spherical absorbing particle undergoing monochromatic coherent illumination and outline a simple method for calculating the image produced by the particle. Calculated results based on the theoretical model are compared to experimentally observed images for both in-focus and out-of-focus 50 μm diameter water droplets, and implications to particle sizing are discussed.

2. PROBLEM FORMULATION

In formulating the physical problem to be solved, we begin with the actual experimental arrangement shown in Fig. 1. The N_2 laser is propagating in the $+z$ direction and is assumed, for calculation purposes, to be linearly polarized in the x direction. Although the output beam of the N_2 laser is inherently randomly polarized, we assume as a first approximation that the coherence length of the N_2 laser is such that at any instant of time the particle is essentially illuminated by a linearly polarized plane wave. The spherical particle, of arbitrary radius a, located at plane z_0 is assumed to be isotropic, homogeneous, and nonmagnetic and to possess a finite electrical conductivity. Accepting that the laser/aerosol interaction can be modeled as a linearly polarized plane wave incident on a spherical absorbing particle, the electromagnetic field distribution can be obtained everywhere internal and external to an absorbing spherical particle using the classic Lorenz-Mie theory.[10,11] A more recent outline of the theoretical details of the derivation can be found in Born and Wolf.[12] The equations used for the external electric field calculations are shown in the appendix. These equations yield exact knowledge (within numerical accuracy) of the electromagnetic field at every point within the aperture located at plane z_1. Although we use the most general form of the Lorenz-Mie equations for calculations presented in this paper, it is possible that simplifications,[12] for specific cases of droplet size, optical properties, or imaging system geometry, can be incorporated into the analysis.

To remain consistent with the scalar diffraction theory outlined by Goodman,[13] we assume that the x-component (direction of polarization) of the electric field will be the only significant electric field component throughout the imaging system. The validity of this assumption can be readily verified by examining the magnitude of the three field components at the aperture (plane z_1).

In addition, the actual physical problem depicted in Fig. 1 can be simplified based on several experimental observations. For the aperture size of 5.5 mm used in the imaging system, it was observed that the particle image at plane z_3 was not significantly affected as the aperture was moved toward the lens. This observation is not entirely unexpected since, with λ being much less than r_a and the distance z_2 to z_1 not being excessively large, we would expect that diffraction effects would be small in proceeding from plane z_1 to z_2. If we neglect diffraction effects due to the aperture, then the aperture serves only to decrease the effective lens diameter. As the aperture size becomes small, however, this assumption is no longer valid. For calculations presented in this paper, the aperture is assumed to be positioned directly in front of the lens. This simplification results in elimination of a very time-consuming numerical integration that would be required to proceed from plane z_1 to z_2.

One also observes that the particle image formed on the vidicon (plane z_3) appears essentially symmetric with respect to the z axis. Although it is apparent that the electric field components will be functions of angle as well as radial location (see the appendix), the angular dependence of the x-component of the electric field has been found to be very weak based upon direct computation. Therefore, we assume that the x-component of the electric field can be treated as axisymmetric. This simplification allows field calculations to be performed in the radial direction only. It is also apparent that since the x-component of the electric field is axisymmetric for a specific incident polarization direction, the calculations will also be valid for randomly polarized light in which the direction of polarization is changing in an arbitrary manner. The mathematical details incorporating the above discussion are presented in the following section.

3. THEORETICAL MODEL

The geometry for the simplified model is shown in Fig. 2. In the following discussion the x-component of the external electric field is denoted by E_m, where the subscript refers to the field evaluated at plane z_m. As discussed previously, the electric field at plane z_1 is known exactly from Lorenz-Mie theory (see the appendix). E_2 can be related to the E_1 by assuming that the paraxial thin lens expression[13] is valid,

$$E_2(x_2,y_2) = \exp(ikn\Delta_0)\exp\left[-\frac{ik}{2f}(x_1^2+y_1^2)\right]E_1(x_1,y_1)$$

$$= \exp(ikn\Delta_0)\exp\left[-\frac{ik}{2f}(x_2^2+y_2^2)\right]E_1(x_2,y_2)\ , \qquad (1)$$

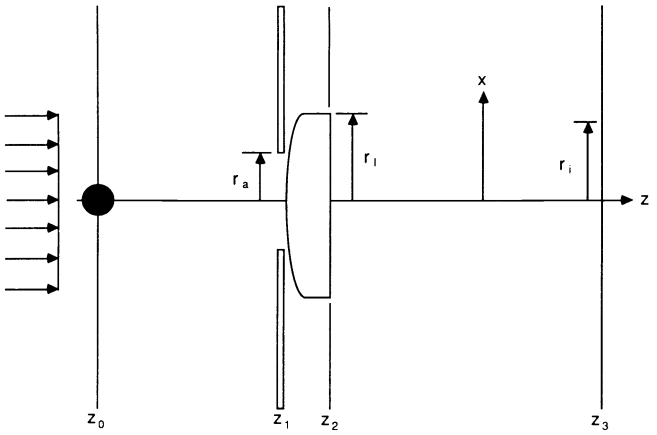

Fig. 2. Simplified geometry used for calculations.

where f is the focal length of the lens, Δ_0 is the thickness of the lens, and $k = 2\pi/\lambda$. By thin lens, we mean that the thickness of the lens is such that a light ray enters and leaves the lens at essentially the same x-y coordinates, thus making (x_1,y_1) and (x_2,y_2) interchangeable. Note that the lens in the imaging system is assumed to be ideal and free from any aberrations. Using the Fresnel approximation[13] in proceeding from plane z_2 to z_3,

$$E_3(x_3,y_3) = \frac{\exp[ik(z_3-z_2)]}{i\lambda(z_3-z_2)} \iint_A E_2(x_2,y_2) \times \exp\left\{\frac{ik}{2(z_3-z_2)}[(x_3-x_2)^2 + (y_3-y_2)^2]\right\} dx_2dy_2 \ . \quad (2)$$

Substituting Eq. (1) into Eq. (2),

$$E_3(x_3,y_3) = \frac{\exp[ik(z_3-z_2)]}{i\lambda(z_3-z_2)} \iint_A \exp(ikn\Delta_0) \exp\left[-\frac{ik}{2f}(x_2^2+y_2^2)\right] \times E_1(x_2,y_2) \exp\left\{\frac{ik}{2(z_3-z_2)}[(x_3-x_2)^2 + (y_3-y_2)^2]\right\} dx_2dy_2 \ . \quad (3)$$

For convenience, Eq. (3) can be written in terms of r-ϕ coordinates (i.e., $x_m = r_m\cos\phi_m$ and $y_m = r_m\sin\phi_m$ for plane z_m),

$$E_3(r_3,\phi_3) = \frac{\exp[ik(z_3-z_2)]}{i\lambda(z_3-z_2)} \int_0^{2\pi}\int_0^{r_a} \exp(ikn\Delta_0) \times \exp\left\{-\frac{ik}{2f}[(r_2\cos\phi_2)^2 + (r_2\sin\phi_2)^2]\right\} \times E_1(r_2,\phi_2) \exp\left\{\frac{ik}{2(z_3-z_2)}[(r_3\cos\phi_3 - r_2\cos\phi_2)^2 + (r_3\sin\phi_3 - r_2\sin\phi_2)^2]\right\} r_2dr_2d\phi_2 \ . \quad (4)$$

Based on the experimental observations discussed earlier, we utilize the axisymmetric field assumption and let $E_1(r_2,\phi_2) = E_1(r_2)$ only. Also, since we will ultimately be concerned only with intensity at plane z_3, constant phase factors can be omitted, giving

$$E_3(r_3,\phi_3) = \frac{1}{i\lambda(z_3-z_2)} \int_0^{r_a} E_1(r_2)\, r_2 \exp\left(-\frac{ik}{2f}r_2^2\right) \int_0^{2\pi} \exp\left\{\frac{ik}{2(z_3-z_2)} \times [r_3^2 + r_2^2 - 2r_2r_3\cos(\phi_2-\phi_3)]\right\} d\phi_2dr_2 \ . \quad (5)$$

In addition to simplifying the electric field description, the axisymmetric assumption also allows exact evaluation of the angular integral in Eq. (5). Utilizing orthogonality along with the identity[13]

$$\exp(ia\sin x) = \sum_{k=-\infty}^{\infty} J_k(a)\exp(ikx) \ , \quad (6)$$

Equation (5) can be simplified, giving

$$E_3(r_3) = \frac{2\pi}{i\lambda(z_3-z_2)} \exp\left[\frac{ikr_3^2}{2(z_3-z_2)}\right] \int_0^{r_a} E_1(r_2)J_0(\beta) \times \exp\left\{-\frac{ikr_2^2}{2}\left[\frac{1}{f} - \frac{1}{(z_3-z_2)}\right]\right\} r_2dr_2 \ , \quad (7)$$

where J_0 is the Bessel function of the first kind of order zero and

$$\beta = \frac{kr_2r_3}{(z_3-z_2)} \ . \quad (8)$$

In terms of intensity at the image plane, Eq. (7) can be written

$$I_3(r_3) = E_3(r_3)E_3^*(r_3) = \left[\frac{2\pi}{\lambda(z_3-z_2)}\right]^2 \left| \int_0^{r_a} E_1(r_2)J_0(\beta) \times \exp\left\{-\frac{ikr_2^2}{2}\left[\frac{1}{f} - \frac{1}{(z_3-z_2)}\right]\right\} r_2dr_2 \right|^2 \ , \quad (9)$$

where the asterisk denotes the complex conjugate. To remain consistent with the Lorenz-Mie theory development (see the appendix), Eq. (9) is written in terms of dimensionless variables,

$$\tilde{I}_3(\tilde{r}_3) = \left[\frac{\alpha}{(\tilde{z}_3-\tilde{z}_2)}\right]^2 \left| \int_0^{\tilde{r}_a} \tilde{E}_1(\tilde{r}_2)J_0(\tilde{\beta}) \times \exp\left\{\frac{-i\alpha\tilde{r}_2^2}{2}\left[\frac{1}{\tilde{f}} - \frac{1}{(\tilde{z}_3-\tilde{z}_2)}\right]\right\} \tilde{r}_2d\tilde{r}_2 \right|^2 \ , \quad (10)$$

where

$$\tilde{\beta} = \frac{\tilde{r}_2\tilde{r}_3\alpha}{(\tilde{z}_3-\tilde{z}_2)} \ , \quad \alpha = \frac{2\pi a}{\lambda} \ , \quad \tilde{r} = \frac{r}{a} \ , \quad \tilde{z} = \frac{z}{a} \ , \quad \tilde{f} = \frac{f}{a} \ . \quad (11)$$

4. RESULTS AND DISCUSSION

To determine whether the theoretical model provided results consistent with experimental observations, the N_2 laser imaging system was configured in a manner identical to Fig. 2. The 50 μm diameter spherical water droplets were generated using

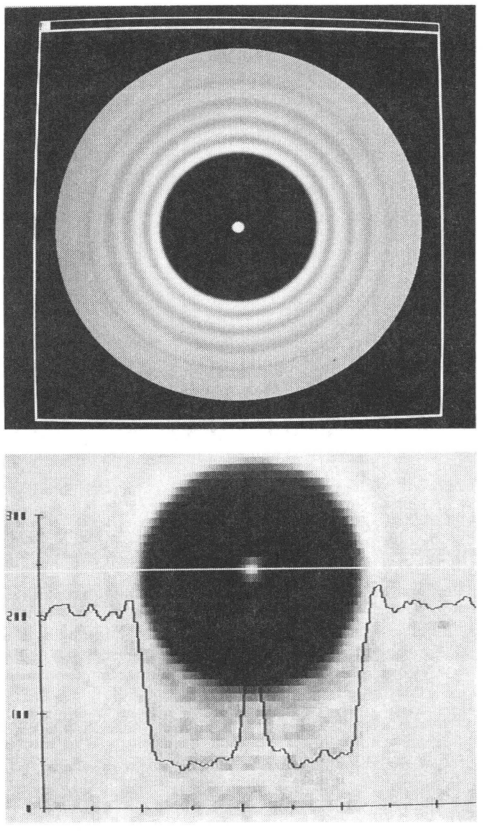

Fig. 3. 50 μm diameter water droplet located at the focal point ($\tilde{z}_1 - \tilde{z}_0 = 2100$, $\tilde{r}_a = 110$). Theoretical calculations (top); observed image (bottom).

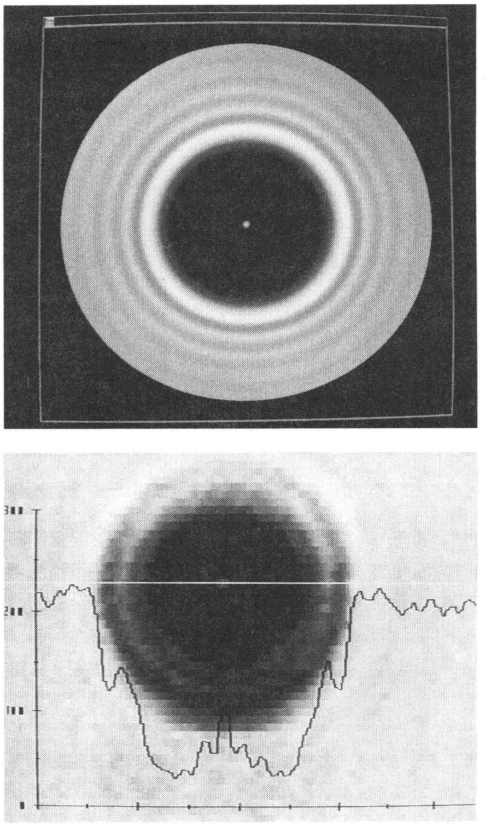

Fig. 4. 50 μm diameter water droplet moved out of focus 10 radii toward the lens ($\tilde{z}_1 - \tilde{z}_0 = 2090$, $\tilde{r}_a = 110$). Theoretical calculations (top); observed image (bottom).

a vibrating orifice generator (TSI model 3450) and allowed to fall in the $-x$ direction through the N_2 laser imaging system at a velocity of approximately 8 m/s. The particle location and the aperture size could be changed using micrometer positioners and a variable size aperture. Unless otherwise noted, the following parameter values, corresponding to the actual experimental arrangement, were used for the computations: radius of water droplet a = 25 μm, incident wavelength λ = 337 nm, complex refractive index[14] $\bar{n} = 1.345 + 8.7 \times 10^{-9}i$, size parameter α = 466, lens focal length $\tilde{f} = 2000$, distance from particle to aperture $(\tilde{z}_1 - \tilde{z}_0) = 2100$ (in-focus case), distance from lens to image plane $(\tilde{z}_3 - \tilde{z}_2) = 42{,}000$, radius of aperture $\tilde{r}_a = 110$, radius of lens $\tilde{r}_\ell = 500$, radius of image $\tilde{r}_i = 50$.

For comparison, we examined four specific cases. Figures 3 through 6 show photographs of both the experimentally observed images obtained using the N_2 imaging system and the theoretically calculated intensities for a 50 μm diameter water droplet located at the focal point ($\tilde{z}_1 - \tilde{z}_0 = 2100$, $\tilde{r}_a = 110$), 10 radii toward the lens ($\tilde{z}_1 - \tilde{z}_0 = 2090$, $\tilde{r}_a = 110$), 10 radii away from the lens ($\tilde{z}_1 - \tilde{z}_0 = 2110$, $\tilde{r}_a = 110$), and 12 radii away from the lens with a decreased aperture size ($\tilde{z}_1 - \tilde{z}_0 = 2112$, $\tilde{r}_a = 40$), respectively. The theoretical images were generated and displayed on a DEC Microvax II/GPX workstation and represent relative intensity values in the image plane for $\tilde{r} = r/a$ values from 0 to 2.5 (i.e., the dark outer circular edge corresponds to 2.5 particle radii). The experimental images are displayed on a video monitor and represent a digitized, enlarged picture of the particle image. Although the quality of the experimental image is limited by the resolution of the imaging system (1 pixel = 1 μm and 256 gray levels), several interesting comparisons can be made.

As expected for an in-focus droplet, Fig. 3 shows a sharply defined boundary in both the theoretical and experimental images. Also evident is the bright center spot appearing in both photographs. The graph superimposed on the experimental image corresponds to the intensity distribution through the diameter of the particle, defined by the horizontal white line. Note that the actual droplet size is the same in both the theoretical and experimental images. The apparent difference results from the discrete amounts of enlargement obtainable using the image processor.

As the droplet is moved out of focus 10 radii toward the lens ($\tilde{z}_1 - \tilde{z}_0 = 2090$), the experimental image, shown in Fig. 4, again exhibits a relatively bright center spot. In addition, two concentric rings of lesser intensity appear near the center spot as well as one ring slightly inside the boundary of the droplet. There also is a slight increase in light intensity just outside the edge of the particle. These general features are also observed in the theoretical calculations.

Figure 5 shows the same size water droplet but moved out of focus 10 radii away from the focusing lens ($\tilde{z}_1 - \tilde{z}_0 = 2110$). Note that both the experimental and theoretical images show less intense ring structure internal to the particle edge than a corresponding particle moved an equal distance toward the lens. The difference in intensity distributions exhibited by particles that are an equal distance out of focus but on opposite sides of the object plane of the lens has been observed previously[6,7] and becomes more significant as the particle size decreases. The

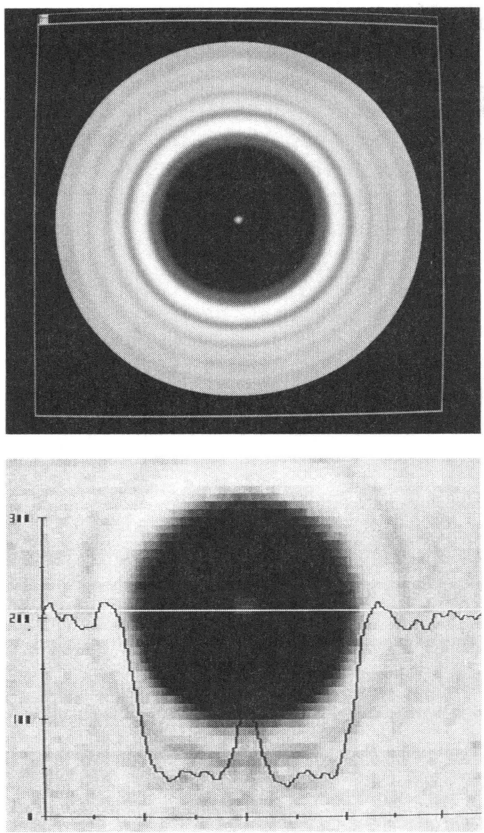

Fig. 5. 50 μm diameter water droplet moved out of focus 10 radii away from the lens ($\tilde{z}_1 - \tilde{z}_0 = 2110$, $\tilde{r}_a = 110$). Theoretical calculations (top); observed image (bottom).

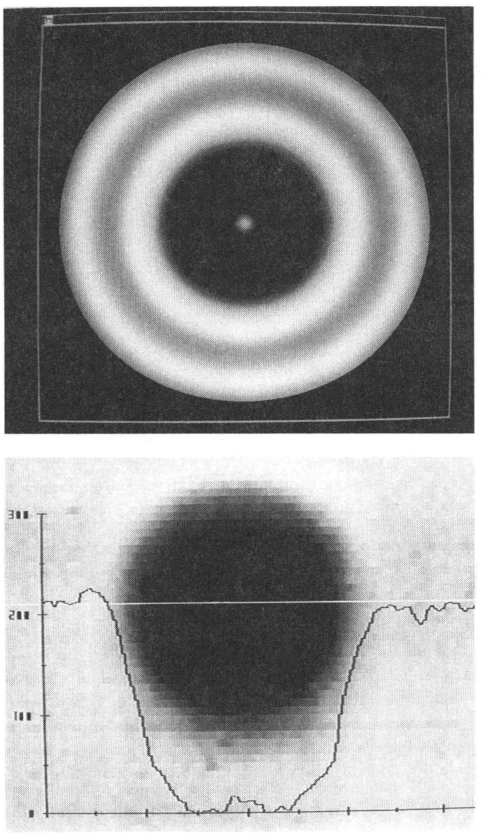

Fig. 6. 50 μm diameter water droplet moved out of focus 12 radii away from the lens and with decreased aperture size ($\tilde{z}_1 - \tilde{z}_0 = 2112$, $\tilde{r}_a = 40$). Theoretical calculations (top); observed image (bottom).

intensity external to the edge of the particle, however, appears to be very similar for the two cases.

As a final case, Fig. 6 shows an out-of-focus particle moved 12 radii away from the lens ($\tilde{z}_1 - \tilde{z}_0 = 2112$) along with a decreased aperture size ($\tilde{r}_a = 40$). In this case, both the theoretical and experimental images show evidence of a blurred particle edge as well as a significant decrease in the spatial frequency of the diffraction rings. The images differ, however, in the intensity of the center spot, which appears brighter for the theoretical calculations than for the experimental image.

In general, the theoretical calculations for all of the cases presented show center intensities higher than the intensities observed experimentally. Also apparent in the experimental images are the slightly different intensity distributions observed on the top and bottom of the droplet as compared to the left and right sides of the droplet. Several factors may contribute to the observed differences between experiment and theory. Among these are the simplified incident beam description used to model the laser pulse, the existence of lens aberrations, which were neglected in the present analysis, the assumption of symmetry about the z axis, the simplified lens transformation, and the relatively high velocity of the droplets (8 m/s) in the vertical direction.

To obtain a more quantitative representation of the effect of droplet location on the calculated intensities, plots of normalized intensity as a function of normalized radial location are shown in Figs. 7 and 8 for 50 μm diameter water droplets as they are moved out of focus toward the lens and away from the lens, respectively. Note that the intensity values are normalized by the maximum intensity for the focal point (in-focus) case. In both figures, it is evident that the intensity gradient near the particle edge decreases significantly as the particle is moved out of focus. As pointed out previously[9,13] for coherent imaging systems, the actual particle edge corresponds to approximately 0.25 the incident intensity. Also evident are the high intensities that appear near the center of the droplet. This high intensity, commonly referred to as Poisson's spot, is approximately four times the intensity of the incident light for the in-focus case ($\tilde{z}_1 - \tilde{z}_0 = 2100$). As already noted, the intensity distribution is not the same for particles an equal distance on each side of the object plane. This fact adds additional uncertainty to the already difficult problem of sizing dynamic sprays.

We also see that below a certain threshold intensity value, the average intensity internal to the particle edge increases as the particle is moved out of focus. This observation is consistent with the concept of using measured average gray level as an indication of the degree of particle defocus. The optimum threshold value for the system described in Fig. 1 was determined[6] experimentally to be approximately one-half the incident intensity.

Figure 9 shows the effect of changing aperture size for a fixed particle location ($\tilde{z}_1 - \tilde{z}_0 = 2112$). Readily apparent is the decrease in spatial frequency of the relative intensity maximum as the aperture size is decreased. This effect should be expected since a decreasing effective lens size serves to restrict the lens to collection of low-frequency portions of the object only. We

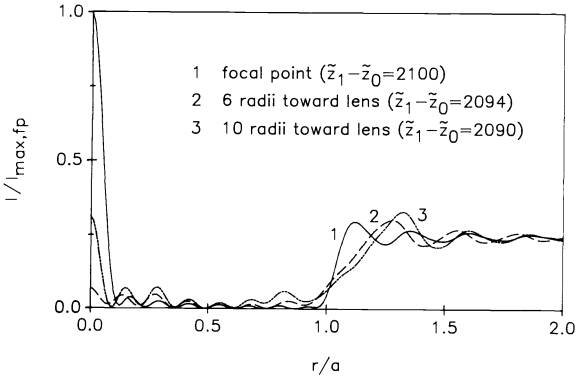

Fig. 7. Normalized intensity as a function of normalized radial position for a 50 μm diameter water droplet moved out of focus toward the focusing lens with r_a = 110.

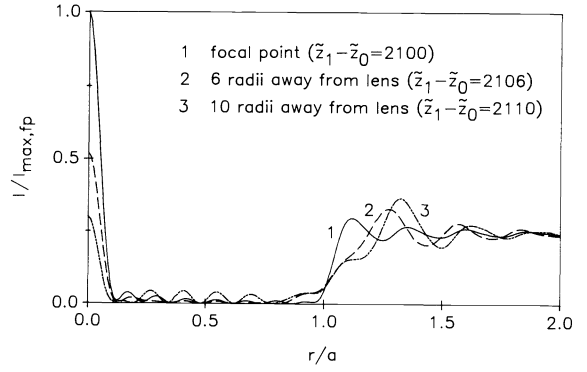

Fig. 8. Normalized intensity as a function of normalized radial position for a 50 μm diameter water droplet moved out of focus away from the focusing lens with r_a = 110.

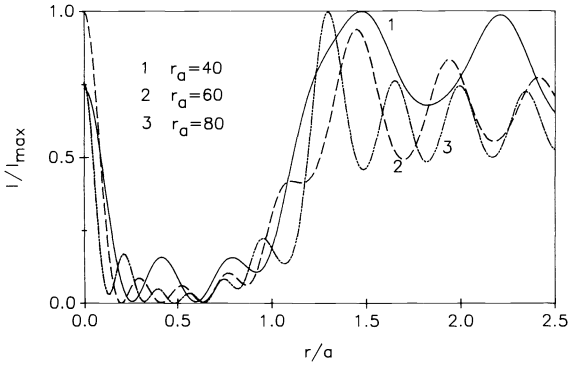

Fig. 9. Normalized intensity as a function of normalized radial position for a 50 μm diameter water droplet moved out of focus 12 radii away from the lens ($\tilde{z}_1 - \tilde{z}_0$ = 2112) using various aperture sizes.

also see that the smaller aperture sizes result in smaller intensity gradients near the particle edge.

5. CONCLUSIONS

Although the theoretical model presented has been simplified extensively over the actual physical problem, the results agree qualitatively with experimental observations. For the cases examined, the locations of the higher intensity diffraction rings agree well with experimental observations. The theoretical model provides results that confirm the validity of using the particle edge intensity gradient and the measured average gray level as focus criteria for the sizing of dynamic particle sprays. The theoretical approach can also be easily extended to more complex imaging system geometries involving multilens systems and to situations in which the axisymmetric field assumption is not appropriate, such as off-axis imaging.

6. APPENDIX

This section presents the near-field Lorenz-Mie theory equations for the scattered, incident, and external electric fields for a spherical particle illuminated by a plane wave, with the following assumptions:

(1) Stationary, homogeneous, isotropic, absorbing sphere of radius a in a homogeneous, isotropic, nonabsorbing medium.
(2) Both the particle and the medium are nonmagnetic (μ = 1).
(3) Particle is illuminated by a plane, monochromatic electromagnetic wave of unit amplitude linearly polarized in the x direction, propagating in the +z direction.
(4) All time-dependent quantities are assumed to vary as $\exp(-i\omega t)$.

6.1. Scattered field

$$\tilde{E}_r^{(s)} = \frac{\cos\phi}{(\alpha\tilde{r})^2} \sum_{\ell=1}^{\infty} \ell(\ell+1) a_\ell \xi_\ell^{(1)}(\alpha\tilde{r}) P_\ell^{(1)}(\cos\theta) \ , \tag{A1}$$

$$\tilde{E}_\theta^{(s)} = -\frac{\cos\phi}{\alpha\tilde{r}} \sum_{\ell=1}^{\infty} \left[a_\ell \xi_\ell^{(1)\prime}(\alpha\tilde{r}) P_\ell^{(1)\prime}(\cos\theta)\sin\theta - b_\ell \xi_\ell^{(1)}(\alpha\tilde{r}) P_\ell^{(1)}(\cos\theta) \frac{i}{\sin\theta} \right] , \tag{A2}$$

$$\tilde{E}_\phi^{(s)} = -\frac{\sin\phi}{\alpha\tilde{r}} \sum_{\ell=1}^{\infty} \left[a_\ell \xi_\ell^{(1)\prime}(\alpha\tilde{r}) P_\ell^{(1)}(\cos\theta) \frac{1}{\sin\theta} - i b_\ell \xi_\ell^{(1)}(\alpha\tilde{r}) P_\ell^{(1)\prime}(\cos\theta)\sin\theta \right] . \tag{A3}$$

The external scattering coefficients a_ℓ and b_ℓ are given by

$$a_\ell = \frac{i^{(\ell-1)}(2\ell+1)}{\ell(\ell+1)} \frac{\psi_\ell'(\bar{n}\alpha)\psi_\ell(\alpha) - \bar{n}\psi_\ell(\bar{n}\alpha)\psi_\ell'(\alpha)}{\bar{n}\psi_\ell(\bar{n}\alpha)\xi_\ell^{(1)\prime}(\alpha) - \psi_\ell'(\bar{n}\alpha)\xi_\ell^{(1)}(\alpha)} \ , \tag{A4}$$

$$b_\ell = \frac{i^{(\ell-1)}(2\ell+1)}{\ell(\ell+1)} \frac{\bar{n}\psi_\ell'(\bar{n}\alpha)\psi_\ell(\alpha) - \psi_\ell(\bar{n}\alpha)\psi_\ell'(\alpha)}{\psi_\ell(\bar{n}\alpha)\xi_\ell^{(1)\prime}(\alpha) - \bar{n}\psi_\ell'(\bar{n}\alpha)\xi_\ell^{(1)}(\alpha)} \ , \tag{A5}$$

where ψ_ℓ, χ_ℓ, and $\xi_\ell^{(1)} = \psi_\ell - i\chi_\ell$ are the Ricatti-Bessel functions, which are related to the Bessel functions of half-integer order; $P_\ell^{(1)}$ is the associated Legendre function of order 1; $\bar{n}$ is the complex refractive index of the sphere; $\alpha = 2\pi a/\lambda$ is the size parameter; and $\tilde{r} = r/a$ is the normalized radial coordinate. Primed quantities denote differentiation with respect to the argument of the function. Note that all electric field quantities are normalized based on an assumed uniform incident electric field of unit magnitude.

The technique used to compute the Ricatti-Bessel functions is described in detail by Ross.[15] Computation of the associated

Legendre function is accomplished by using standard recursion formulas such as those presented by Abramowitz and Stegun.[16]

6.2. Incident field

$$\tilde{E}_r^{(i)} = \exp(i\alpha\tilde{r}\cos\theta)\sin\theta\cos\phi \ , \tag{A6}$$

$$\tilde{E}_\theta^{(i)} = \exp(i\alpha\tilde{r}\cos\theta)\cos\theta\cos\phi \ , \tag{A7}$$

$$\tilde{E}_\phi^{(i)} = -\exp(i\alpha\tilde{r}\cos\theta)\sin\phi \ . \tag{A8}$$

6.3. External field

In terms of Cartesian coordinates,

$$\tilde{E}_x^{ext} = (\tilde{E}_r^{(i)} + \tilde{E}_r^{(s)})\sin\theta\cos\phi + (\tilde{E}_\theta^{(i)} + \tilde{E}_\theta^{(s)})\cos\theta\cos\phi - (\tilde{E}_\phi^{(i)} + \tilde{E}_\phi^{(s)})\sin\phi \ , \tag{A9}$$

$$\tilde{E}_y^{ext} = (\tilde{E}_r^{(i)} + \tilde{E}_r^{(s)})\sin\theta\sin\phi + (\tilde{E}_\theta^{(i)} + \tilde{E}_\theta^{(s)})\cos\theta\sin\phi + (\tilde{E}_\phi^{(i)} + \tilde{E}_\phi^{(s)})\cos\phi \ , \tag{A10}$$

$$\tilde{E}_z^{ext} = (\tilde{E}_r^{(i)} + \tilde{E}_r^{(s)})\cos\theta - (\tilde{E}_\theta^{(i)} + \tilde{E}_\theta^{(s)})\sin\theta \ . \tag{A11}$$

7. REFERENCES

1. W. M. Farmer, "Measurements of particle size, number density, and velocity using a laser interferometer," Appl. Opt. 11(11), 2603–2612 (1972).
2. W. D. Bachalo and M. J. Houser, "Phase/Doppler spray analyzer for simultaneous measurements of drop size and velocity distributions," Opt. Eng. 23(5), 583–590 (1984).
3. D. R. Alexander, K. J. Wiles, S. A. Schaub, and M. P. Seeman, "Effects of non-spherical drops on a phase doppler spray analyzer," in *Particle Sizing and Spray Analysis,* N. Chigier and G. W. Stewart, eds., Proc. SPIE 573, 67–72 (1985).
4. B. A. Weiss, P. Derov, D. DeBiase, and H. C. Simmons, "Fluid particle sizing using a fully automated optical imaging system," Opt. Eng. 23(5), 561–566 (1984).
5. K. D. Ahlers and D. R. Alexander, "Microcomputer based digital image processing system developed to count and size laser-generated small particle images," Opt. Eng. 24(6), 1060–1065 (1985).
6. K. J. Wiles, "Development of a system for secondary liquid injection into a mach 2 supersonic flow to study drop size and distribution by video imaging techniques," master's thesis, Univ. of Nebraska, Lincoln (1985).
7. M. P. Seeman, "Aerosol spray characterization using a PDPA and laser imaging/video processing system," master's thesis, Univ. of Nebraska, Lincoln (1987).
8. E. D. Hirleman, "Calibration standard reticles for particle sizing instruments," Laser ElectroOptics Ltd. product announcement RR-50.0-3.0-0.08-102-CF-No. 114 (1982).
9. B. J. Thompson and P. H. Malyak, "Accuracy of measurement in coherent imaging of particulates in a three-dimensional sample," in *Particle Sizing and Spray Analysis,* N. Chigier and G. W. Stewart, eds., Proc. SPIE 573, 12–20 (1985).
10. G. Mie, "Bieträge zur Optik trüber Medien, speziell kolloidaler Metallösungen," Ann. Phys. 25, 377–445 (1908).
11. P. Debye, "Der Lichtdruck auf Kugeln von beliebigem Material," Ann. Phys. 30, 57–136 (1909).
12. M. Born and E. Wolf, *Principles of Optics,* 6th Edition, Pergamon Press, Oxford, England 633–664 (1987).
13. J. W. Goodman, *Introduction to Fourier Optics,* McGraw-Hill, New York (1968).
14. G. M. Hale and M. R. Querry, "Optical constants of water in the 200-nm to 200-μm wavelength region," Appl. Opt. 12(3), 555–563 (1973).
15. W. D. Ross, "Computation of Bessel functions in light scattering studies," Appl. Opt. 11(9), 1919–1923 (1973).
16. M. Abramowitz and I. A. Stegun, eds., *Handbook of Mathematical Functions,* pp 332–334, Dover, New York (1972).

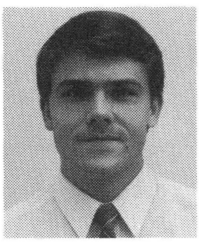

Scott A. Schaub received his BS degree in mechanical engineering in 1985 and his MS degree in 1986 from the University of Nebraska-Lincoln. He is currently working toward his Ph.D. degree in energetics and mechanics. His research interests include high energy laser interaction with solid and liquid aerosols and dynamic particle size measurements. He is a member of the OSA.

Dennis R. Alexander is a professor and director of the Center for Electro-Optics in the Mechanical Engineering Department at the University of Nebraska-Lincoln. Dr. Alexander received his degrees from Kansas State University in nuclear engineering. His research has been in the area of applied optical measurements. Of particular interest is the in situ sizing and characterization of aerosols using laser imaging techniques coupled with computer digital image processing algorithms. His research interests also include the theoretical modeling and the experimental interaction of high energy lasers with aerosols. Dr. Alexander has been a visiting scientist at Los Alamos Scientific Laboratory and Amoco Oil Company Research Facility. He is a member of the Fine Particle Society, the American Society of Mechanical Engineers, the American Nuclear Society, the American Society for Engineering Education, and SPIE.

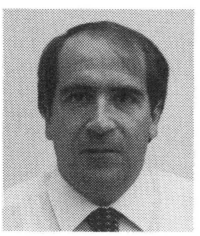

John P. Barton received his BS degree in mechanical and aerospace engineering from the University of Missouri-Columbia in 1973 and his MS and Ph.D. degrees in mechanical engineering from Stanford University in 1974 and 1980, respectively. Currently, Dr. Barton is an assistant professor within the Mechanical Engineering Department at the University of Nebraska-Lincoln, where he is associated with the Center for Electro-Optics. Dr. Barton's research interests include the experimental and theoretical analysis of general laser beam/aerosol particle interactions.